CFD INVESTIGATION OF THE EFFECT OF SPINNERET GEOMETRY ON THE FLOW BEHAVIOR OF MULTIPHASE POLYMERIC FLUIDS
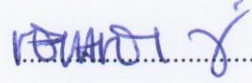
by

DİLAY ÜNAL

Submitted to the Graduate School of Engineering and Natural Sciences
in partial fulfillment of
the requirements for the degree of
Master of Science
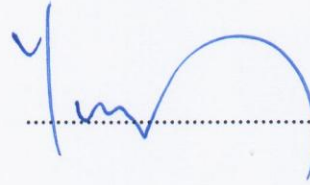
Sabancı University
August 2014

CFD INVESTIGATION OF THE EFFECT OF SPINNERET GEOMETRY ON THE FLOW BEHAVIOR OF MULTIPHASE POLYMERIC FLUIDS

APPROVED BY:

Assoc. Prof. Dr. Mehmet Yıldız ....

(Thesis Supervisor)

Prof. Dr. Yusuf Z. Menceloğlu ....

(Thesis Supervisor)

Assoc. Prof. Dr. Ali Koşar ....

Asst. Prof. Dr. Fevzi Cebeci ....

Asst. Prof. Dr. Serkan Ünal ....

DATE OF APPROVAL :   06/08/2014

"Of course there is no formula for success, except perhaps an unconditional acceptance of life and what it brings."

Arthur Rubinstein

CFD Investigation of the Effect of Spinneret Geometry on the Flow Behavior of Multiphase Polymeric Fluids

Dilay Ünal

ABSTRACT

Nano or micro particle integrated polymeric fibers are commonly produced via so-called wet spinning process. During the process, particle containing polymer solution is exposed to high shear stresses while passing through the spinneret holes, and high shear stresses give rise to increased viscosity (shear thickening). In the present work, it was aimed to investigate parameters that affect the flow behavior of shear thickening fluids. The fluid considered in the simulations was prepared by dispersing silica nanoparticles in poly(ethyleneglycol), and the resulting fluid was a complex fluid which shows shear thinning until a certain shear rate, and above that shear rate it shows shear thickening. The effects of various parameters on the flow properties of the fluid have been investigated over a wide range of conditions. The variables studied are: geometry (reservoir depth, channel length, contraction width, edge roundness), velocity (0.02-0.12 m/s). A two-dimensional simulation model based on an Eulerian-Eulerian multiphase approach is considered to simulate particle containing polymeric fluid. The governing equations and constitutive relations for both phases are solved using the finite volume method, by employing the FLUENT software of ANSYS Workbench. Since it would be computationally too expensive to model the entire spinneret, only one single hole was considered as the computational domain. It was found that reservoir depth and channel length have slight effect on the viscosity but at the same time contraction width and roundness of the edge of the contraction has a significant effect on the viscosity profile. Besides, by increasing velocity fluid viscosity increased as well.

Spinneret Geometrisinin Çok Fazlı Polimerik Akışkanların Akış Özellikleri Üzerine Etkilerinin Hesaplamalı Akışkanlar Dinamiği Yöntemi ile İncelenmesi

Dilay Ünal

MAT, M.Sc. Tezi, 2014

Tez Danışmanları : Prof. Dr. Yusuf Menceloğlu, Doç. Dr. Mehmet Yıldız

Anahtar Kelimeler : Hesaplamalı Akışkanlar Dinamiği, FLUENT, çok fazlı akış

ÖZET

Nano veya mikro boyutta parçacık içeren polimerik fiberler, yaş çekim yöntemi adı verilen bir proses ile üretilebilmektedir. Bu proses esnasında, parçacık içeren polimer solüsyonu, spinneret (düze) adı verilen mikron boyutlarındaki deliklerden geçirilirken, yüksek kayma gerilimine maruz kalırlar. Polimer solüsyonu üzerine etki eden bu yüksek kayma gerilimi viskozite artışına sebep olur. Bu tez kapsamında, kayma kalınlaşması gösteren polimerik sıvıların akış özelliklerine etki eden parametreler incelenmiştir. Simülasyonlarda kullanılan akışkan, silika nanoparçacıklarının poli(etilenglikol) içerisinde dağıtılmasıyla hazırlanmış olup, hazırlanan bu numune, belirli bir kayma geriliminin altında kayma incelmesi gösterirken, o kayma geriliminin üzerinde ise kayma kalınlaşması göstermektedir. İncelenen parametreler: geometri (rezervuar derinliği, kanal uzunluğu, kısılma alanının genişliği, ve köşelerin yuvarlatılması), akış hızı (0.03-0.12 m/s). Simülasyonlar iki boyutlu bir geometri kullanılarak, Eulerian-Eulerian metodu kullanılarak modellenmiştir. Akış özelliklerini tanımlayan denklemler, sonlu hacimler metodu kullanılarak, ANSYS FLUENT programı ile çözülmüştür. Simülasyonların maliyeti düşünülerek, tüm spinnereti modellemek yerine, yalnızca bir adet delik baz alınmış ve hesaplamalar onun üzerinde yapılmıştır. Elde edilen sonuçların ışığında, rezervuar derinliği ve kanal uzunluğunun viskozite üzerine çok az etkisi olduğu görülmüştür. Bunun yanında, kısılma alanının genişliği ve köşelerin keskinliğinin ise viskozite profili üzerinde hatırı sayılır ölçüde değişikliğe sebep olduğu gözlemlenmiştir. Ayrıca, akış hızının artırılmasıyla da viskozitenin önemli ölçüde arttığı görülmüştür.

ACKNOWLEDGEMENTS

TABLE OF CONTENTS

LIST OF FIGURES

LIST OF TABLES

ABBREVIATIONS

CFD	Computational Fluid Dynamics
ODT	Order-Disorder Transition
PEG	Poly(ethyleneglycol)
UDF	User Defined Function
2D	Two Dimensional

To my beloved mom...

CHAPTER 1

INTRODUCTION

1.1. Motivation

Natural fibers such as cotton, wool, and silk have been used by humans since ancient times. Patenting of artificial silk in 1885 was a milestone which started the modern fiber industry. Man-made fibers include materials such as nylon, polyester, rayon, and acrylic. The combination of strength, weight, and durability have made these materials very important in modern industry [1].

Synthetic polymers have been developed that possess superior characteristics, like high softening point to allow for ironing, high tensile strength, stiffness, and desirable fabric qualities. These polymers are then formed into fibers with various characteristics. Fibers are very important applications of polymeric materials. From textiles to bullet-proof vests, fibers have become very important in the modern life. As the technology of fiber processing expands, new generations of strong and light weight materials will be produced [2].

Studies on the new generation fiber composites that contain nanoparticle additives have been significantly increased over the last decade. Enhancing the thermal performance and physical strength of fluids by using nanoparticles was a main motivation for creating these composites [3].

The process of producing fibers is called spinning. There are three types of spinning, namely, melt, dry and wet. All of these methods involve a forced fluid flow through the process equipment called spinneret, which consists of hundreds or thousands of micron size holes. During the process, particle containing polymer solution is exposed to high shear stresses while passing through the spinneret holes, and high shear stresses give rise to increased viscosity (shear thickening) [4].

The shear thickening phenomena has drawn interest over the last 40 years, which is mainly due to the fact that it may cause damage to the processing equipment and dramatic change in suspension microstructure, such as particle aggregation.

For an industrial manufacturing process, it is crucial to maintain continuous production without losing quality of the product. Yet, it is known that nanoparticle containing fluids imperils the fiber production process by harming the process equipments, clogging or narrowing micro channels, due to the shear thickening, arisen from the particle aggregation and coagulation. This causes an enormous and intolerable loss of time and money for companies; therefore, addressing this problem remains as of great importance. CFD aided studies for investigating various types of multiphase fluid flow problems in close conduits and open channels have been increasingly used because of the advantages that they provide like rapid evaluation of multiphase flow problems under a wide range of conditions, which is almost impossible experimentally [5-7].

In light of the above discussion, the motivation behind this study is to investigate and understand the processing parameters which promote shear thickening inside the channels of die. To this end, in this study, we have numerically scrutinized the effects of die geometry and velocity on the flow behavior of shear thickening fluids.

1.2. Outline of the Thesis

The rest of this thesis continues as follows. Section 2 briefly provides some information about the basics of rheology, and CFD method for multiphase fluid flows. Shear thickening phenomenon as well as some relevant studies dedicated to explain this phenomenon are discussed in Section 2. In this section, a number of pertinent CFD studies are also cited and briefly summarized. In section 3, the governing equations and constitutive relations used to numerically model the problem in question are provided in detail. Geometry, mesh, material properties and numerical methods are described in Section 4. Results of the numerical study are discussed in Section 5. The present work is concluded with final remarks and the future work in Section 6.

CHAPTER 2

BACKGROUND

2.1. Rheology Basics

Fluids having direct proportionality between shear stress (σ) and shear rate ($\dot{\gamma}$) under a simple shear are called as "Newtonian Fluids". The behavior of these types of fluids are expressed by a relation of the form given in equation (1) where μ is the viscosity, which does not depend on the shear rate but might depend on the external factors like temperature and pressure. Most low-molecular-weight materials like organic and inorganic liquids, molten metals and gases exhibit Newtonian behavior under a simple shear [8].

$$\sigma_{xy} = \mu * \dot{\gamma}, \tag{1}$$

Fluids with non-proportional relationship between shear stress and shear rate are referred to non-Newtonian fluids. Shear rate dependent viscosity is one of the most important characteristic features of these fluids, where viscosity is time-independent but depends on the type and rate of deformation. These fluids can be either shear-thinning (pseudo-plastic), where viscosity decreases with increasing shear rate or shear-thickening (dilatant) where viscosity increases with increasing shear rate. Fluids exhibiting a combination of shear thinning and shear thickening behavior are so-called complex fluids [9].

Shear thinning and shear thickening fluids have been intensely studied and investigated by both academy and industry over the last few decades. Shear thinning is the most widely encountered type of time-independent non-Newtonian fluid behavior in engineering practice and the physics behind shear thinning is far more established compared to shear thickening. [10]

Shear thickening fluids can have supreme applications like shock absorbing and force damping skis, tennis rackets and flexible body armor when they are engineered into composite materials, but yet they may harm the process equipments by clogging the pipes or spraying equipments. Many colloidal suspensions, such as dies, paints,

3

coatings, and lubricants, are subjected to high shear rates during processing. Sometimes, shear rate is high enough to drive shear thickening, which means viscosity increases discontinuously with small increases in shear rate. This behavior can damage processing equipment and provoke changes in the suspension microstructure such as driving irreversible flocculation and particle aggregation [11, 12].

Many theories have been suggested in the literature in order to explain the origin of the shear thickening phenomena. In the early 1970s, Hoffman claimed that, shear thickening is a consequence of an order-to-disorder transition (ODT) of the fluid. Below a certain shear rate, a colloidal fluid is ordered into layers, and with the applied shear, this layered arrangement prevents collisions of colloidal particles and thus reduces viscosity. Above the critical shear rate, the layered arrangement is disrupted by intense hydrodynamic forces. As a consequence, increased collisions give rise to the dramatically elevated viscosity. Hoffman confirmed this theory with his light-scattering experiments [13].

Even though the ODT theory was well accepted and the study pioneered the curiosity towards the shear thickening, thereafter, many studies have been done in this field in order to further understand the physics behind the shear thickening phenomena. In a review article that Barnes published in 1989, the author claimed that shear thickening occurs in all dispersion systems, but this thickening is too marginal in some dispersions to be detected with conventional rheometers. Nevertheless, shear thickening in some dispersions is so severe and hence can easily be detected with rheometers. According to Barnes, the parameters affecting shear thickening are: particle size, particle size distribution, particle shape, particle volume fraction, particle-particle interaction, continuous phase viscosity, and the type, rate and time of deformation. All of these parameters have been studied in the literature so far [14, 15].

Some of the studies claimed that order-disorder transition is not necessary for shear thickening. They claimed that suspensions that had a disordered arrangement of particles at the very beginning, and even suspensions that contain only 2 particles which have Brownian motion, may show shear thickening [11].

The non-Newtonian rheological behavior, e.g., shear thickening and/or shear thinning, can be captured using simple equations relating viscosity and shear rate via minimum number of parameters. Some of these equations are namely, the Carreau Model, the

Cross Model, the Power-Law Model and the Herschel-Bulkley Model. All of those models are capable of capturing the fluid as either shear thickening or shear thinning fluid. However, some non-Newtonian fluids show divergent behavior between shear thickening and shear thinning. These so-called complex fluids, act as shear thinning fluids below a certain shear rate, and above that shear rate they act as shear thickening fluids. There is no model reported in the literature that is able to capture the complex viscosity behavior [16, 17]. It is of great importance to handle the viscosity profile of a fluid of interest, accurately. Accordingly, the lack of the constitutive equations regarding the complex fluids leaves a challenge behind. In the present study, this challenge has been attempted to be addressed.

2.2. Computational Fluid Dynamics for Multiphase Fluid Flows

In the field of polymeric materials, computers have been intensively used for industrial and research applications. In particular, computational fluid dynamics (CFD) of polymeric fluids has received growing attention for understanding the physics of processes, thereby making it possible to design better equipments and optimize the processing conditions [18].

The foundation of the CFD software are based on the principles of fluid mechanics, together with improved numerical methods for the solution of the governing equations and constitutive relations, which describe the rheological behavior of fluid and particles if involved [18].

Most of the flow problems encountered in industrial processes involve complex kinematics due to different geometries, combined shear and elongation, different time dependences and amplitudes of deformations [18]. The physical phenomena of a problem considered in this thesis work, are governed by partial differential equations, which are rather complex for having analytical solutions, and hence need to be discretized numerically. Numerical discretization is transformation of the partial differential equations into linear sets of equations which can then be solved by using appropriate numerical methods via computer programming. There are three main mesh based numerical discretization techniques, namely, finite difference method, finite element method and finite volume method [7, 19]. In this study, FLUENT software of ANSYS Workbench is used and FLUENT uses the finite volume method for discretization of partial differential equations.

5

CFD aided studies for investigating various types of multiphase fluid flow problems in close conduits and open channels have been increasingly used. Main advantage of CFD aided studies is that three dimensional solid–liquid two phase flow problems under a wide range of flow conditions may be evaluated rapidly, which is almost impossible experimentally. Particle processing, conveying and separation are of crucial importance in industrial processes. Besides empirical correlations and experimental investigations, numerical simulations have gained significant attention in studying particle containing flows. There are quite much of studies in the literature involving the particle containing flows [7].

In computational simulations, regardless of the method being used for handling the problem of particulate fluid flow, it is mandatory to cover the dominant flow regimes of the process accurately. For instance, Ristic *et al.* simulated the multiphase flow in ventilation mill, ventilation channel and centrifugal separator. They started to simulate the flow by using Eulerian-Eulerian approach and showed that their numerical model did not show any convergent behavior because of the complex geometry and large number of grids. Then they have used the mixture model and the Eulerian-Lagrangian approach, and obtained results which are in good agreement with the experimental results. Their study also showed the importance of using the right approach for handling the flow problem [20, 21].

Employing a specific multiphase model (the discrete phase, mixture, Eulerian model) to handle the momentum transfer depends on the volume fraction of solid particles and on the fulfillment of the requirements, which enable the selection of a given model. The problem that we investigate is a diluted system. Therefore the discrete phase model, the mixture model and the Eulerian model are appropriate in this case. The Eulerian model has two versions, namely granular version and the non-granular version. Granular version is preferable in our case since non-granular version does not include models for handling friction and collisions between particles into account which is believed to be of importance in nanoparticulate fluids [22].

Most of the studies, regarding to the nanoparticle containing multiphase flows found in the literature, have dealt with the heat transfer properties of the flows by using CFD methods. Abbassi *et al.* modeled forced convection of laminar nanofluids flowing trough microchannels by using Eulerian-Eulerian multiphase model and FLUENT

software. They investigated the influence of concentration and size nanoparticles on the Nusselt number and pressure drop [23]. Kamali and Binesh numerically investigated multi-wall carbon nanotube (MWCNT) based nanofluids in a straight tube under constant heat flux condition. They simulated the nanofluid flow passing through the tube by using in-house built numerical code, with the non-Newtonian power-law fluid model and found that the heat transfer coefficient is dominated by the wall region due to non-Newtonian behavior of nanofluid. [24]. Apart from these, one may find quite many studies in the literature, which have focused on the heat transfer properties of nanoparticulate multiphase flows [25-27].

One may find immense many numbers of experimental studies devoted to understand the physics behind the shear thickening phenomena, and the various parameters affecting shear thickening. However, there are a limited number of computational studies in the literature which have focused on the rheological behavior of shear thickening fluids. Out of these computational studies, the majority of the works investigated the heat transfer properties of these fluids or some other properties, and only a few of them computationally investigated the parameters affecting shear thickening, which are of significant importance in fiber spinning processes. This study aims to understand parameters, namely geometry and fluid velocity which potentially affect the shear thickening behavior inside the spinneret in fiber spinning processes.

Barigou *et al.* studied viscous non-Newtonian flow under the influence of a superimposed rotational vibration by employing different fluids of the power-law, Hershel-Bulkley and Bingham plastic types [28]. Chabbra *et al.* investigated numerically two-dimensional laminar flow of power-law fluids past a long square cylinder confined in a planar channel for various Reynolds numbers and blockage ratios. They presented extensive numerical results, to elucidate the effects of blockage, power-law index and Reynolds number on the drag coefficient, stream function, vorticity etc. [29]. Shah and Manzar studied particle conveying Newtonian and non-Newtonian slurries in straight and coiled pipes by using CFD and showed in their studies that shear stress inside the flow domain, increases with increasing values of flow rate, particle size, particle density and particle loading. They also found that there is a good agreement between near-wall particle concentration and particle shear stress [30].

Non-newtonian fluids have a wide variety of applications in the food industry as well. The shear rheology of bread dough was studied by Hicks *et al.* The geometry consisted a sudden contraction where shear rate increased significantly, resulting in increased viscosity. Their results showed that shear rate and viscosity tend to be higher nearby the walls and contraction areas, and this increase in shear rate and viscosity tends to be more tremendous with higher flow rates [31]. Sun and Norton reviewed numerous articles and showed the importance of CFD methods for studying thermal and hydraulic performance of non-Newtonian fluids in food industry like milk, yogurt, soup etc. [32].

CHAPTER 3

FORMULATION OF CFD MODEL

The Eulerian-Eulerian two fluid model was used in the computational studies described within this thesis.

The Eulerian-Eulerian multiphase model assumes that the flow consists of solid *"s"* and fluid *"f"* phases, that are separate yet they form interpenetrating continua, so that $\alpha_f + \alpha_s = 1$, here α_f and α_s are the volumetric concentrations of fluid and solid phases, respectively. The Eulerian-Eulerian model solves two sets of momentum and continuity equations for each phase. Coupling between phases is achieved through the pressure and interphase exchange coefficients. [33]

The laminar flow of non-Newtonian fluid containing nanoparticles is assumed to be governed by the following equations, which form the basis of the Eulerian-Eulerian CFD model used.

3.1. Conservation of Mass

The continuity equation for phase q is:

$$\frac{1}{\rho_{rq}}\left(\frac{\partial}{\partial t}\left(\alpha_q \rho_q\right) + \nabla \cdot \left(\alpha_q \rho_q \vec{v}_q\right) = \sum_{p=1}^{n}(\dot{m}_{pq} - \dot{m}_{qp})\right), \qquad (2)$$

where $\vec{v}_q$ is the velocity of phase q and $\dot{m}_q$ characterizes the mass transfer between p^{th} and q^{th} phase, and $\dot{m}_{pq}$ characterizes the mass transfer from phase q to phase p, and it is possible to specify these mechanisms, separately.

3.2. Conservation of Momentum

The general form of momentum balance for phase q is:

$$\frac{\partial}{\partial t}\left(\alpha_q \rho_q \vec{v}_q\right) + \nabla \cdot \left(\alpha_q \rho_q \vec{v}_q \vec{v}_q\right) = -\alpha_q \nabla p + \nabla \cdot \bar{\bar{\tau}}_q + \alpha_q \rho_q \vec{g} +$$
$$\sum_{p=1}^{n}\left(\vec{R}_{pq} + \dot{m}_{pq}\vec{v}_{pq} - \dot{m}_{qp}\vec{v}_{qp}\right) + \left(\vec{F}_q + \vec{F}_{lift,q} + \vec{F}_{vm,q}\right), \qquad (3)$$

where $\bar{\bar{\tau}}$ is the qth phase stress-strain tensor, and this stress-strain tensor is in the following form:

$$\bar{\bar{\tau}}_q = \alpha_q \mu_q \left(\nabla \vec{v}_q + \nabla \vec{v}_q^T\right) + \alpha_q \left(\lambda_q - \frac{2}{3}\mu_q\right)\nabla \cdot \vec{v}_q \bar{\bar{I}}. \tag{4}$$

Here μ_q and λ_q are the shear and the bulk viscosity of phase q, $\vec{F}_q$ is an external body force, $\vec{F}_{lift,q}$ is a lift force, $\vec{F}_{vm,q}$ is a virtual mass force, $\vec{R}_{pq}$ is an interaction force between phases and p is the pressure shared by the all phases. $\vec{v}_{pq}$ is the interphase velocity.

3.2.1. Fluid-Fluid Momentum Equation

The conservation of momentum for fluid phase q is like the following:

$$\frac{\partial}{\partial t}\left(\alpha_q \rho_q \vec{v}_q\right) + \nabla \cdot \left(\alpha_q \rho_q \vec{v}_q \vec{v}_q\right) = -\alpha_q \nabla p + \nabla \cdot \bar{\bar{\tau}}_q + \alpha_q \rho_q \vec{g} +$$
$$\sum_{p=1}^{n}\left(K_{pq}\left(\vec{v}_p - \vec{v}_q\right) + \dot{m}_{pq}\vec{v}_{pq} - \dot{m}_{qp}\vec{v}_{qp}\right) + \left(\vec{F}_q + \vec{F}_{lift,q} + \vec{F}_{vm,q}\right). \tag{5}$$

Here $\vec{g}$ is the accelaration due to gravity and $\bar{\bar{\tau}}_q$, $\vec{F}_q$, $\vec{F}_{lift,q}$ and $\vec{F}_{vm,q}$ are as defined above.

3.2.2. Fluid-Solid Momentum Equation

The conservation of momentum for the sth solid phase is:

$$\frac{\partial}{\partial t}\left(\alpha_s \rho_s \vec{v}_s\right) + \nabla \cdot \left(\alpha_s \rho_s \vec{v}_s \vec{v}_s\right) = -\alpha_s \nabla p - \nabla p_s + \nabla \cdot \bar{\bar{\tau}}_s + \alpha_s \rho_s \vec{g} +$$
$$\sum_{l=1}^{N}\left(K_{ls}\left(\vec{v}_l - \vec{v}_s\right) + \dot{m}_{ls}\vec{v}_{ls} - \dot{m}_{sl}\vec{v}_{sl}\right) + \left(\vec{F}_s + \vec{F}_{lift,s} + \vec{F}_{vm,s}\right), \tag{6}$$

where p_s is the sth solids pressure, $K_{ls}=K_{sl}$ is the momentum exchange coefficient between fluid or solid phase, where l stands for liquid phase and s for solid phase, N is the total number of phases, and $\vec{F}_s$, $\vec{F}_{lift,s}$ and $\vec{F}_{vm,s}$ are as defined above.

3.3 Carrier Fluid Viscosity

Non-Newtonian flow behavior of the fluid was modeled by using the below given Carreau Model. Where $\dot{\gamma}$ is shear rate, η_∞ is the infinite shear rate viscosity, η_0 is zero shear rate viscosity, λ is relaxation time and n is power index.

$$\eta = \left(\eta_\infty + (\eta_0 - \eta_\infty)[1 + \dot{\gamma}^2 \lambda^2]^{n-1/2}\right). \tag{7}$$

3.4. The Pressure Correction Equation

For incompressible multiphase flow, the pressure-correction equation is in the following form:

$$\sum_{k=1}^{n} \frac{1}{\rho_{rk}} \left\{ \frac{\partial}{\partial t} \alpha_k \rho_k + \nabla \cdot \alpha_k \rho_k \vec{v}_k' + \nabla \cdot \alpha_k \rho_k \vec{v}_k^* - \left(\sum_{l=1}^{n} (\dot{m}_{lk} - \dot{m}_{kl}) \right) \right\} = 0, \tag{8}$$

where ρ_{rk} is the phase reference density for the kth phase (defined as the total volume average density of phase k), $\vec{v}_k'$ is the velocity correction for the kth phase, and $\vec{v}_k^*$ is the value of $\vec{v}_k$ at the current iteration. The velocity corrections are expressed as functions of the pressure corrections.

3.5. Volume Fraction Equation

The description of multiphase flow incorporates the concept of phasic volume fractions, denoted here by α_q. Volume fractions represent the space occupied by each phase, and the laws of conservation of mass and momentum are satisfied by each phase individually [33].

The volume of phase q, V_q, is defined by:

$$V_q = \int_V \alpha_q \, dV, \tag{9}$$

where

$$\sum_{q=1}^{n} \alpha_q = 1. \tag{10}$$

The effective density of phase q is $\hat{\rho}_q = \alpha_q \rho_q$ where ρ_q is the physical density of phase q.

3.6. Fluid-Solid Exchange Coefficient

Within particulate fluid flows, fluid-solid exchange can be described by using many models which were developed empirically, like Gidaspow [34], Syamlal-O'Brian [35], Huilin-Gidaspow [36], Gibilaro [37], and Wen-Yu models. The model developed by Wen and Yu was used in our study, since it is the best choice for systems involving particles less than twenty percent. For the model of Wen-Yu, the fluid-solid exchange coefficient is of the following form:

11

$$K_{sl} = \frac{3}{4} C_D \frac{\alpha_s \alpha_l \rho_l |\vec{v}_s - \vec{v}_l|}{d_s} \alpha_l - 2.65, \tag{11}$$

where C_D is as following:

$$C_D = \frac{24}{\alpha_l Re_s} [1 + 0.15(\alpha_l Re_s)^{0.687}]. \tag{12}$$

In above formulae, α_s and α_l stand for volume fraction of solid and liquid phases respectively. Reynolds number, Re_s, is calculated according to the following equation:

$$Re_s = \frac{\rho_l d_s |\vec{v}_s - \vec{v}_s|}{\mu_l}. \tag{13}$$

3.7. Solid Shear Stresses

The solids stress tensor contains shear and bulk viscosities arising from particle momentum exchange due to translation and collision. A frictional component of viscosity can also be included to account for the viscous-plastic transition that occurs when particles of a solid phase reach the maximum solid volume fraction.

The collisional and kinetic parts and the optional frictional part are added to give the solid shear viscosity:

$$\mu_s = \mu_{s,col} + \mu_{s,kin} + \mu_{s,fr}.. \tag{14}$$

3.7.1. Collisional Viscosity

The collisional part of the shear viscosity is modeled as below, where Θ_s is the granular temperature of solid phase.

$$\mu_{s,col} = \frac{4}{5} \alpha_s \rho_s d_s g_{0,ss} (1 + e_{ss}) \left(\frac{\Theta_s}{\pi}\right)^{1/2} \alpha_s. \tag{15}$$

3.7.2. Kinetic Viscosity

There are two expressions provided by ANSYS FLUENT software for the kinetic part of the shear viscosity which were developed by Syamlal *et al.* [35] and Gidaspow [34] *et al.* The expression derived by Gidaspow was used in our model and is shown below:

$$\mu_{s,kin} = \frac{10\rho_s d_s \sqrt{\Theta_s \pi}}{96\alpha_s(1 + e_{ss})g_{0,ss}}\left[1 + \frac{4}{5}g_{0,ss}\alpha_s(1 + e_{ss})\right]^2 \alpha_s. \tag{16}$$

3.7.3. Bulk Viscosity

The solids bulk viscosity accounts for the resistance of the granular particles to compression and expansion. It has the following form from Lun et al [38].

$$\lambda_s = \frac{4}{3}\alpha_s\rho_s d_s g_{0,ss}(1 + e_{ss})\left(\frac{\Theta_s}{\pi}\right)^{1/2}. \tag{17}$$

3.8. Solver Theory

ANSYS FLUENT solves the governing integral equations for the conservation of mass and momentum. A control-volume-based technique is used that consists of:

• Division of the computational domain into discrete control volumes using a computational mesh.

• Integration of the governing equations on the individual control volumes to construct algebraic equations for the discrete dependent variables such as velocities, pressure, viscosity.

• Linearization of the discretized equations and solution of the resultant linear equation system to obtain updated values of the dependent variables.

The pressure-based solver uses an algorithm, which belongs to a general class of methods called the projection method. In the projection method, wherein the constraint of mass conservation of the velocity field is achieved by solving a pressure correction equation. The pressure correction equation is derived from the continuity and the momentum equations in such a way that the velocity field, corrected by the pressure, satisfies the continuity. Since the governing equations are nonlinear and coupled to one another, the solution process involves iterations wherein the entire set of governing equations is solved repeatedly until the solution converges.

Pressure-based solver is used for low-speed, incompressible flows. Two pressure-based solver algorithms are available in ANSYS FLUENT, namely, segregated algorithm, and coupled algorithm. Pressure-based coupled algorithm is used for multiphase flow

13

problems. The pressure-based coupled algorithm solves a coupled system of equations comprising the momentum equations and the pressure-based continuity equation. With the coupled algorithm, each iteration consists of the steps as outlined below:

1. Update fluid properties (e.g., density, viscosity) based on the current solution.

2. Solve the coupled system of momentum and pressure correction equations, using the recently updated values of pressure, mass flux and velocity field.

3. Correct mass fluxes using the pressure correction obtained from Step 2.

4. Solve the equations for additional scalars, if any, using the current values of the solution variables.

5. Update the source terms arising from the interactions between different phases (e.g., source term for the carrier phase due to discrete particles).

6. Check for the convergence of the equations.

Since the momentum and continuity equations are solved in a closely coupled manner, the rate of solution convergence significantly improves compared to the segregated algorithm. However, the memory requirement increases by $1.5 - 2$ times that of the segregated algorithm since the discrete system of all momentum and pressure-based continuity equations needs to be stored in the memory when solving for the velocity and pressure fields.

CHAPTER 4

DESCRIPTION OF CFD SIMULATIONS

All of the simulations described within this thesis were performed by using ANSYS Workbench Release 14.0 and solved by using the FLUENT solver component of the package.

4.1. Simulation of Validation Case

In order to check the validity and the accuracy of the solver, a reference study by Ease and Barigou has been considered where the numerical modeling of a flow through channels were conducted with the assumptions of 2D, incompressible, isothermal, and fully developed flow. The test case modeled in this work as a validation is a flow through a straight pipe with the diameter and length of 45 mm, and 600 mm, respectively. The geometry was meshed with in total 32000 fine cells. A non-Newtonian power law fluid model given in Equation (18) was used with the consistency index, k, of 0.16 Pa.s^n and power-law index, n, of 0.81. The density of the fluid is 1000 kg/m^3. Velocity inlet boundary condition was used at the inlet with the value of inlet velocity of 0.066 m/s while the zero gauge pressure condition was used at the outlet. Walls were considered to have no-slip boundary conditions.

$$\eta = k\dot{\gamma}^{n-1},$$ (18)

Initially, the fluid without any particles was modeled and the results were compared with the analytical ones. Governing equations were discretized using SIMPLE algorithm and momentum equation was dicretized using second-order upwind differencing scheme. Residual target was 10^{-5} and convergence was reached after approximately 800 iterations at steady state conditions.

The shear thickening fluid containing 30% v/v particles with diameter of 2mm was modeled and the particle velocity results were compared with the ones in the reference paper. Governing equations were discretized using phase coupled SIMPLE algorithm and momentum equation was dicretized using second-order upwind differencing scheme. Residual target was 10^{-4} and convergence was reached after approximately 130 time steps, with 10 iterations at each time step, and with a small time step size as 0.05.

15

4.2. Simulations of Single Phase Fluid Flow and Two-Phase Solid-Liquid Flow

4.2.1. Geometry

A spinneret is multi-pored equipment through which a plastic polymer melt is drawn to form fibers. A representative picture of a spinneret is shown in Figure 1. Spinnerets used in acrylic fiber spinning processes consist of thousands of micron-size pores.

Figure 1. A representative image of a spinneret

Since it would be computationally too expensive and time consuming to model an entire spinneret, a single pore was taken into account and was modeled in two dimensions. Half of a single pore is shown in Figure 2 with dimensions. Only half of the pore was modeled because in 2D right and left boundaries of the pore are symmetric boundaries.
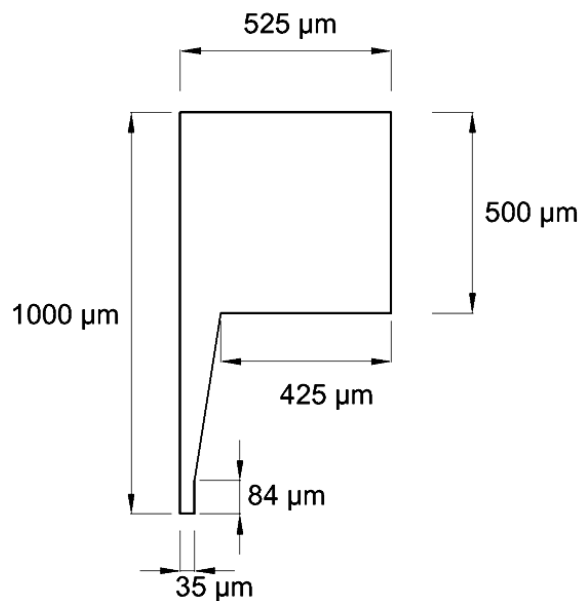

Figure 2. Geometry of the computational domain

4.2.2. Mesh

For two dimensional channel flows, it is recommended to mesh the computational domain with tetrahedral elements. Therefore, the mesh was generated with 9791 tetrahedral elements. The quality of the mesh was 0.9 on a scale from 0 to 1, where 0 and 1 correspond to the lowest and highest quality, respectively.

4.2.3. Material Properties

In the context of this work, it was aimed to investigate the flow behavior of shear-thickening fluids, flowing through tiny spinneret holes. The shear-thickening fluid which was used in simulations was prepared in-house instead of taking an example from the literature. As explained in the second section of this thesis, neat fluids do not show shear thickening. Therefore, nanoparticle embedded shear thickening fluid was prepared.

Yıldız *et al.* showed in their recent paper that silica nanoparticle containing poly(ethyleneglycol) (PEG) solutions show complex rheological behavior [39]. In the light of this study, silica-PEG system was prepared as a baseline fluid with the intention of using the rheological data collected from this system in the simulations. Silica nanoparticles, which were 400 nm in diameter, were dispersed in PEG, molecular weight of 200, by using shear mixer at 1000 rpm for 3 hours. Rheology measurements were conducted afterwards on this sample by using Malvern Bohlin 2000 rheometer. Sample first showed shear thinning at lower shear rates, and then it started to thicken after a certain threshold.

As discussed in Section 2, non-Newtonian fluids can be modeled by using several models like power-law, Carreau and Cross model. However, none of these models are capable of expressing the complex viscosity profile (both shear thinning and thickening). Therefore, a model was needed to introduce the viscosity of a complex fluid to the FLUENT. This was achieved by an in-house developed User Defined Function (UDF). The UDF simply defined the viscosity in two parts. If the shear rate is below the threshold, shear thinning part of the UDF was used by the software, and if the shear rate is above the threshold, shear thickening part of the UDF was used.

Viscosity profile obtained from the rheometer was first splitted into two as shear thinning and shear thickening parts. Afterwards these two parts were curve fitted to the

Carreau Fluid Model which is given in Equation (19) separately by using the Solver module of MS Office Excel. By using the data from the curve fittings, the UDF was developed and the viscosity was introduced to the FLUENT by using it. Carreau model parameters are given in Table 1. The real viscosity profile obtained from the rheometer and curve fitted one are shown in Figure 3. The compatibility of these two curves indicates that Carreau model formed of two parts is a good representative for our fluid sample.

$$\mu = \left(\mu_\infty + (\mu_0 - \mu_\infty)[1 + \dot{\gamma}^2 \lambda^2]^{(n-1)/2}\right). \tag{19}$$

Table 1. Carreau Model Parameters

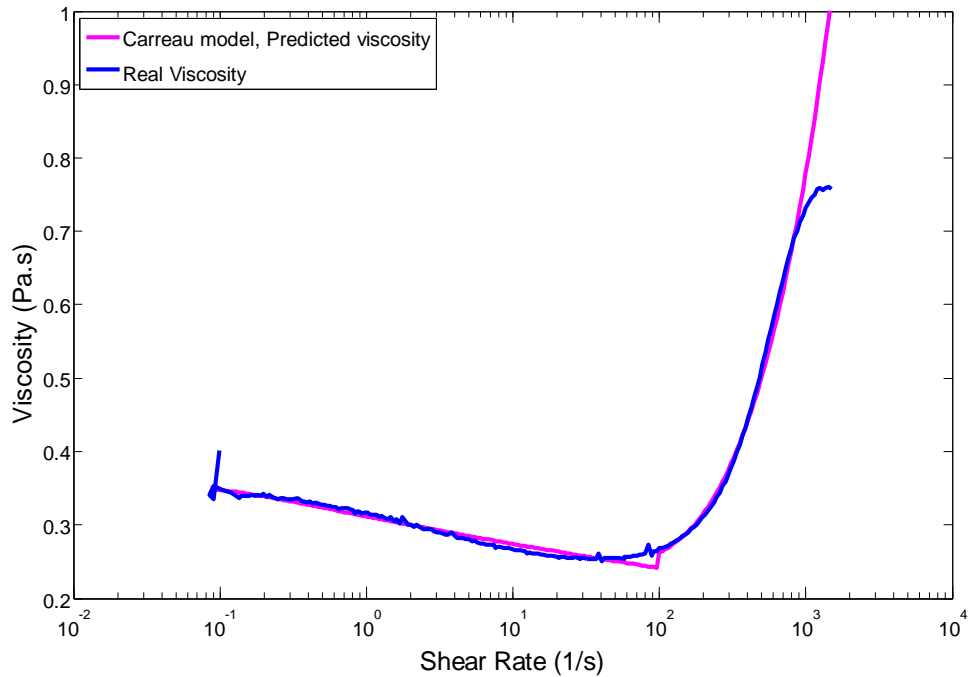| Carreau Model Parameters	Shear Thinning Part	Shear Thickening Part
μ_∞	0	0
μ_0	9,197351	1,873088
λ	20,61487	0,021371
n	0,75726	26,67904

Figure 3. Viscosity profile of the fluid used in simulations as a function of shear rate, and its curve fitting to the Carreau Model

4.2.4. Description of the Numerical Model

As discussed in previous sections, nanoparticles were introduced in the continuous liquid phase as a second Eulerian phase.

18

The boundary conditions at inlet and outlet were the mass flow rate and pressure outlet, respectively. Mass flow rate and particle volume fraction were 0.0185 kg/s and 2% for inlet, respectively. Zero gauge pressure was set for the pressure outlet boundary. Right and left boundaries of the computational domain were the symmetric boundaries. The other parts of the geometry were set as walls. For both liquid and solid phases, no-slip condition was used near the walls. Boundaries of the computational domain are simply shown in Figure 4. Gravitational acceleration was included in the calculations in the opposite direction of the y-axis, where the flow inside the channel is in the positive direction of x-axis.
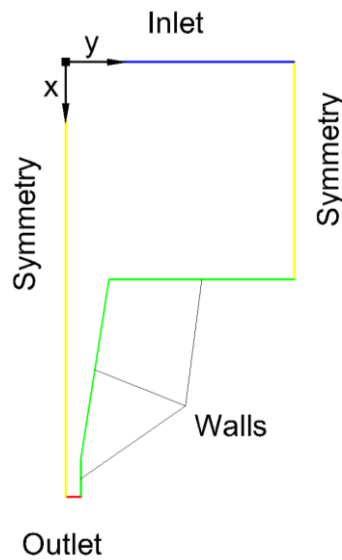

Figure 4. Boundaries of the computational domain

For multiphase flow problems, interparticle interactions and modeling of these forces are of significant importance. The drag force was modeled using the Wen-Yu drag model (Equation (11)). For solid concentrations up to 20% v/v, the Wen-Yu model is preferable. Numerical convergence under steady state mode was too difficult to achieve for solid-liquid flow. Thus, the simulations were run in the transient mode. A small time step of 0.001s was used for the sake of easier convergence. Residual target was set to the 10^{-5} for all solved equations. Governing equations were discretized using the phase coupled SIMPLE algorithm and momentum equation was dicretized using second-order upwind differencing scheme. Momentum equation was gradually relaxed with the factors in the range of 0.7 to 0.3 in order to ease the convergence. On average, 200 time steps were required with 10 iterations per time step, in order to achieve convergence.

CHAPTER 5

RESULTS AND DISCUSSION

5.1. Validation Case

In order to ensure the validation and reliability of the commercial code, the study of Ease and Barigou [40] was taken as a reference. The results were duplicated and they were compared with the analytical results obtained by using equations (20) and (21) [41].

The volumetric flow rate, Q, of a power law fluid is given by the following equation

$$Q = \frac{n\pi R^3}{(3n + 1)}\left(\frac{R}{2k}\frac{\Delta p}{L}\right)^{1/n},$$ (20)

where R is the pipe radius, and $\Delta P/L$ is the pressure drop per unit length. The fluid velocity profile can be derived by using the following relation where r is radial position.

$$v(r) = \frac{n}{n + 1}\left(\frac{\Delta pR}{2kL}\right)^{1/n} R\left[1 - \left(\frac{r}{R}\right)^{(n+1)/n}\right].$$ (21)

All of the variables in Eq. (20) are known including, Q, n, k and R. By inserting all of these known variables into the equation, pressure drop per unit length was calculated. Then this calculated pressure drop were inserted into the Eq. (21), and by giving different values to the r, velocities across the radius were analytically calculated. These analytical results were compared to the ones that were obtained from the simulations and the results are given in Figure 5.

Single phase flow simulations were performed for two different cases, where power-law parameters and inlet velocity were changed. Analytical and CFD results for these two cases were exactly the same as it is shown in Figure 5. This situation indicates that the commercial CFD code that we used is capable of modeling non-Newtonian single phase flows and the results obtained from the code are reliable. Multiphase flow simulations were done for 30% v/v particle containin shear thickening fluid. The particle velocity results are given in Figure 6, which are in excellent agreement with that given in the reference paper of by Ease and Barigou [40]. These simulations confirmed the validity and reliability of the commercial CFD code.

20
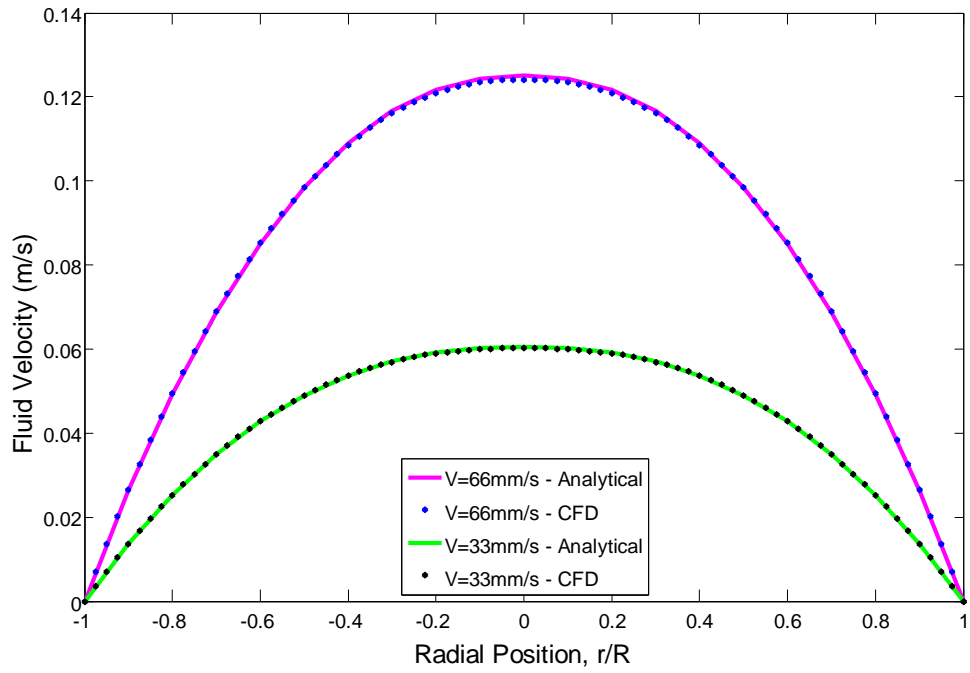
Figure 5. Comparison of analytical and CFD velocity profiles for a power law fluid flowing alone: (k=0.16 Pa.s^n, n=0.81), V_{in}=66mm/s; (k=0.75 Pa.s^n, n=0.71), V_{in}=33mm/s
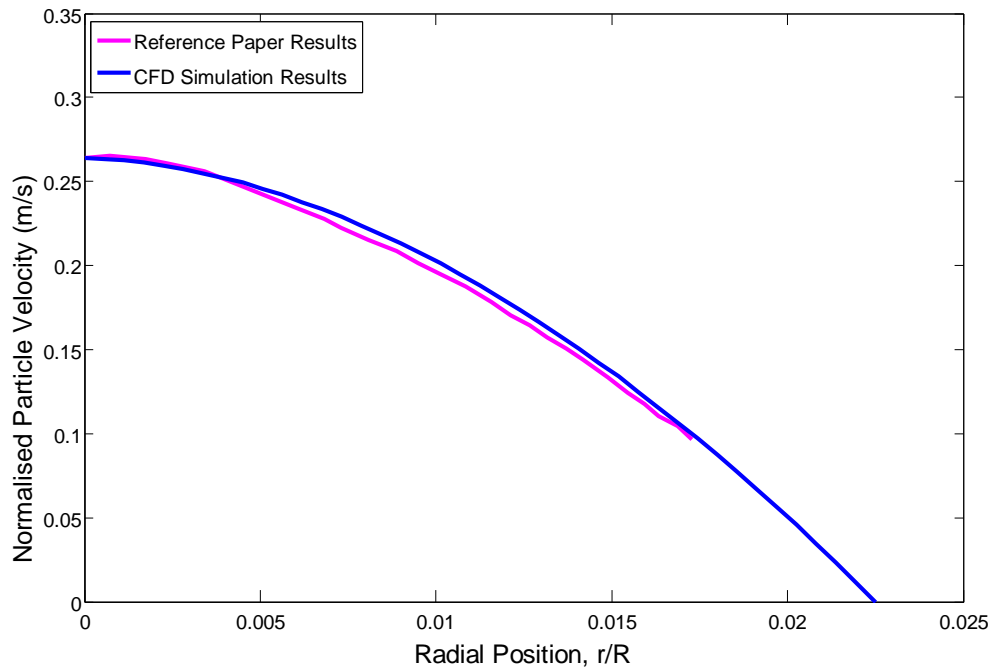

Figure 6. Normalised solid-phase velocity profile in shear thickening carrier fluid: (k=0.75 Pa.s^n, n=0.71); d=2mm, ρ_s=1020 kg/m^3, C_s=0.30; V_{in}= 125 mm/s

5.2. Two-Phase Solid-Liquid Flow

5.2.1. Mesh Dependency Analysis

The mesh independence tests involve refining the initial mesh by increasing the number of cells present in the initial mesh by approximately 1-3 folds. For the standard geometry (case 1, details given in Table 2), mesh size of 2797 cells was first refined to 11188 cells and then to 25173 cells, for the entire geometry. There was no further improvement found in simulations results, after the number of cells has been increased from 2797 to 11188 and 25173. Therefore, optimum mesh was assumed to be the one containing 2797 cells and it was computationally the most economical option. Same mesh dependence study were also done on the altered geometries as well (cases 2 to 9, details given in Table 2), and it was found that refinements didn't change the simulations results. Therefore, non-refined meshes were used for each case.

5.2.2. Parametric Study

Initial simulations were conducted on the standard geometry with a standard inlet velocity and particle loading as described in section 3.2.1. Afterwards, changes were made in the geometry in order to understand the effect of the geometry on the flow behavior and viscosity of the fluid. Besides, it is known from the literature that fluid and/or particle velocity also affects the shear rate and viscosity. Therefore, different inlet velocities were used in simulations in order to observe their effects on the viscosity.

5.2.2.1. Geometry

In order to investigate the effect of the geometry to the flow behavior of multiphase fluid, various forms of the initial geometry were created by modifying certain sections (denoted by the letters a, b and c) of the initial geometry as shown in Figure 7. In Table 2, parameters of these sections are shown in detail. Other sections of the geometry have remained unchanged noting that there are some process induced constrains for the spinneret geometry such as the hole sizes that controls the fiber diameter.

In order to see the relative change of viscosity more clearly compared to the zero shear rate viscosity, viscosity profiles were normalized using the zero shear viscosity. Viscosity profiles are shown across the contraction, and along the spinneret close to the

symmetry boundary, and these sections are denoted as Line 1 and Line 2 as shown in Figure 7.
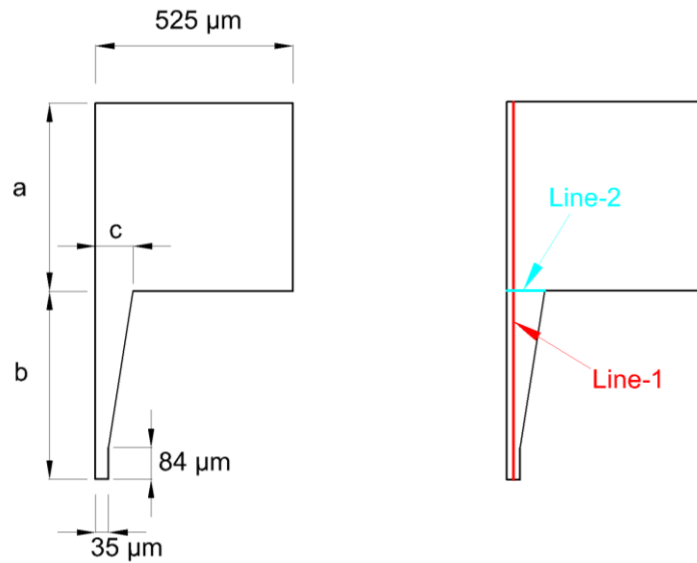

Figure 7. Parts of the geometry that were changed and lines that viscosity was observed

Table 2. Dimensions of the geometry used at simulations

Parametric Study	Case Number	a (μm)	b (μm)	c (μm)
Reservoir Depth	1	500	500	100
	2	600	500	100
	3	700	500	100
Channel Length	4	500	600	100
	5	500	700	100
Contraction Width	6	500	500	150
	7	500	500	200
Corner Rounding				Circle Radius
	8	500	500	50
	9	500	500	100

Here, initially, the results obtained upon changing reservoir depth will be presented for both along Line-1 and Line-2. The Figure 8 and Figure 9 give the variation of the fluid viscosity along the Line-1 and Line -2 of the computational geometry for different reservoir depth.
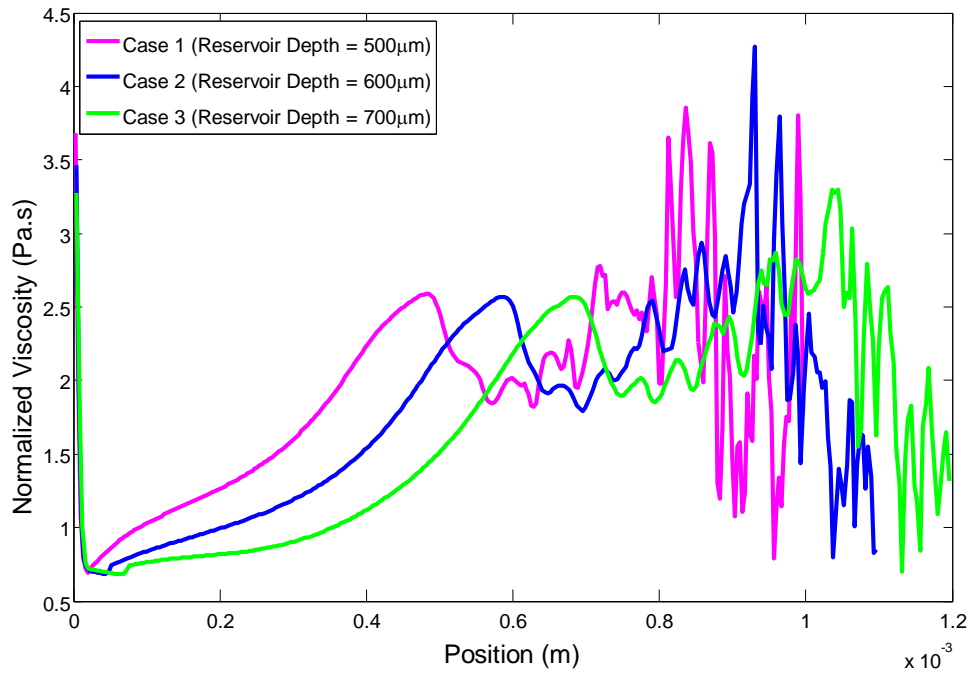
23

Figure 8. Effect of the reservoir depth on the viscosity profile along the Line-1
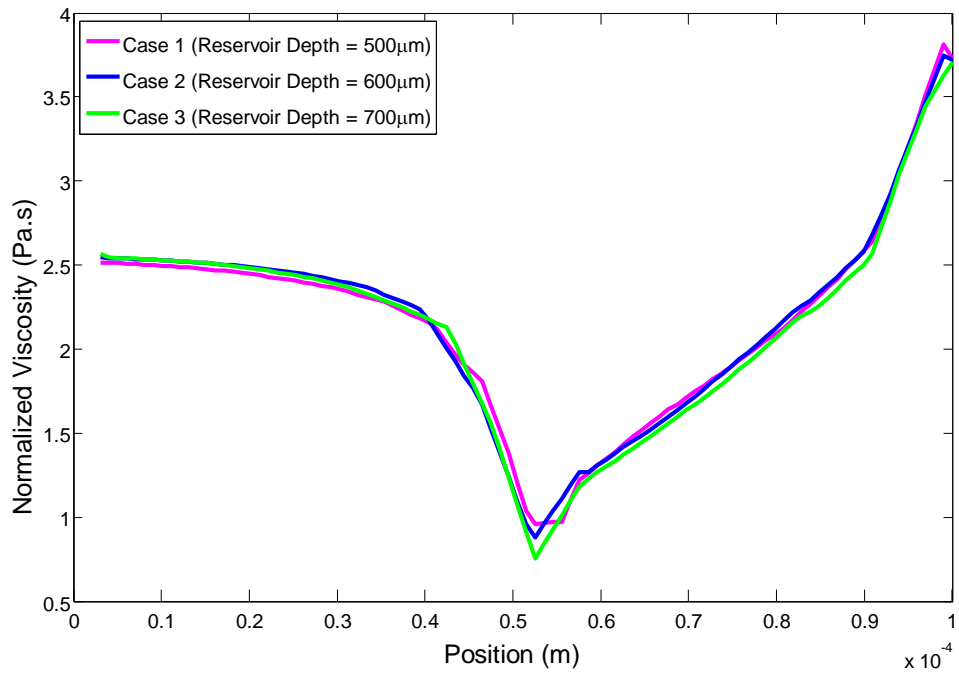

Figure 9. Effect of the reservoir depth on the viscosity profile across the contraction

24

As seen from the Figure 8, the viscosity starts to increase inside the spinneret up to reaching to contraction section, which can be easily justified recalling Hagen–Poiseuille equation where the viscosity is linearly proportional to pressure difference. Getting closer towards the contraction, pressure difference gets bigger and bigger as seen in Figure 12, which gives the contour plot of total pressure, and this leads to increase in the viscosity up to a value nearly 2.5 times greater than the zero shear viscosity. After the sudden contraction, pressure drop as well as the shear rate along the Line-2 decreases, thereby resulting in the decline in the viscosity. Roughly at a distance of 0.1 mm after the contraction, viscosity profile starts to fluctuate due to the pressure drop and fluid acceleration inside the channel, hence leading to local non uniformities in the velocity field and in turn fluctuating viscosity profile. This trend was also observed for all the cases investigated within the scope of this thesis. Note that upon increasing the reservoir depth, the spatial position for the onset of the contraction changes. Therefore, in Figure 8, the first peak point in viscosity versus position moves to the right in the graph. Otherwise, one can conclude from the figure that the viscosity profile is not affected by the reservoir depth. As for the viscosity variation along Line 2, one can see from Figure 9 that there is sharp decrease in the viscosity away from the left symmetry axis since the velocity gradient and in turn the shear rate is small therein. Towards the wall, the velocity gradient and shear rate increases due to the no-slip boundary condition, and hence viscosity starts rising up significantly, reaching to a value which is nearly 3.5 times greater than the zero shear viscosity. Moreover, one may note the viscosity profile along Line-2 is also independent of the reservoir depth as expected.

In Figure 10 and Figure 11, which yield the viscosity variation along the Line-1 and Line-2 respectively, we have scrutinized the effect of channel length on the viscosity profile. Figure 10 and Figure 11 both reveal that the viscosity profile is not affected by the channel length significantly except that upon increasing channel length, the peak viscosity value at the vertical position of 0.5 given in Figure 10 increases slightly, which is due to the decrease in the pressure gradient along the channel length in the vicinity of the contraction.
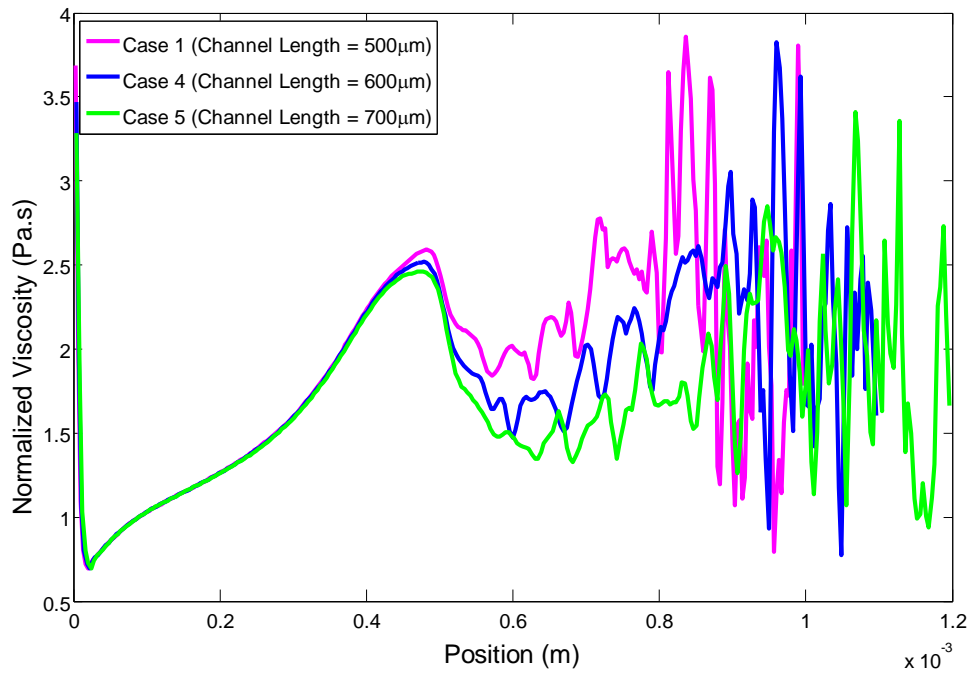
Figure 10. Effect of the channel length on the viscosity profile along the Line-1
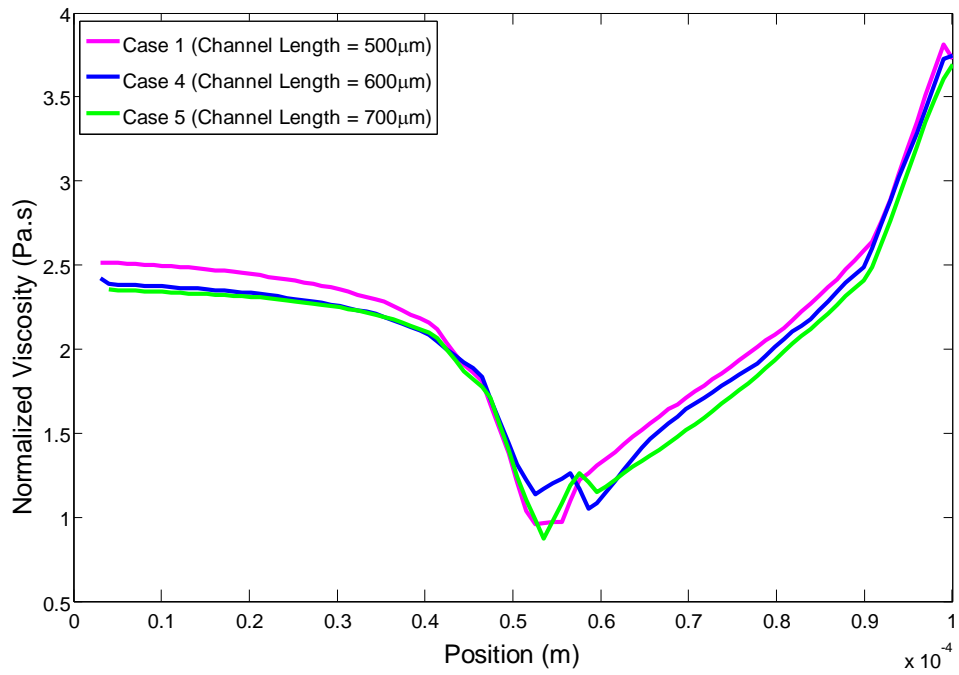

Figure 11. Effect of the channel length on the viscosity profile across the contraction
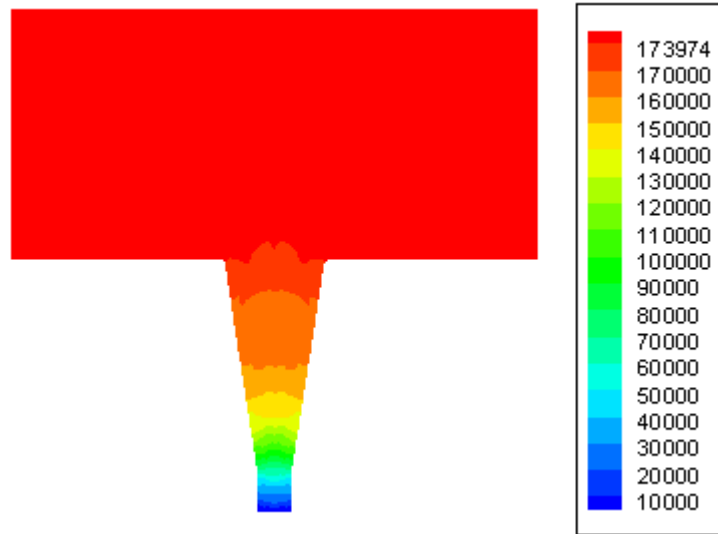
26

Figure 12. Total pressure contours of the mixture

In Figure 13 and Figure 14 the viscosity profiles along Line-1 and Line-2 are provided for three different channel widths namely, 100μm to 150μm and 200μm. It can clearly be seen from Figure 13 and Figure 14 that widening the contraction section results in a decrease in viscosity, which is due to the fact that when the contraction is larger, pressure and velocity gradients become less severe, hence causing lower viscosities.

Having observed that narrower contraction results in drastic increase in viscosity values, for the sake of completeness, it becomes prudent to shed some light on the effect of corner geometry on the viscosity profile. To this end, we have also modeled the current initial geometry with two different round corners having radius of 50μm and 100μm. For these simulations, viscosity profiles are shown in Figure 15 and Figure 16 shows that around contraction area, viscosity increases with increasing corner roundness. Figure 16 verifies this situation but also it shows that viscosity across contraction decreases significantly. The increase in the viscosity near to the symmetry boundary is due to the increased pressure gradient therein. Nevertheless Figure 16 shows that the viscosity decreases significantly across the contraction, especially at closer parts to the corner, as a result of drastic decrease in the velocity gradient and shear rate, as well. For case 9, where the contraction is the smoothest, viscosity at the edge decreases to half compared to the standard case 1. These results show that, the roundness of a corner of a contraction is of great importance for optimizing spinneret geometry.
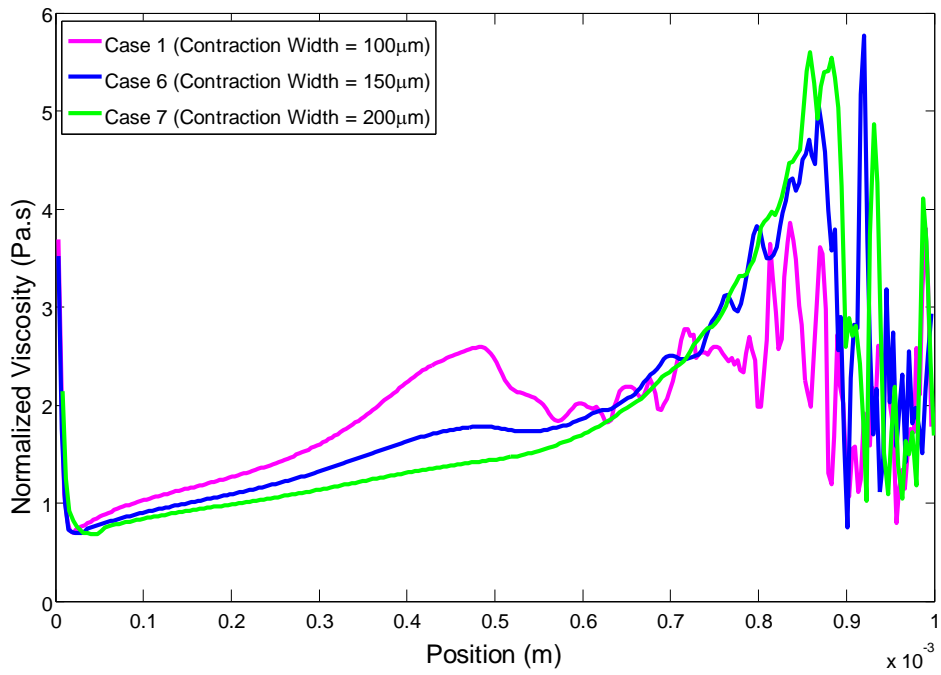
27

Figure 13. Effect of the contraction width on the viscosity profile along the Line-1
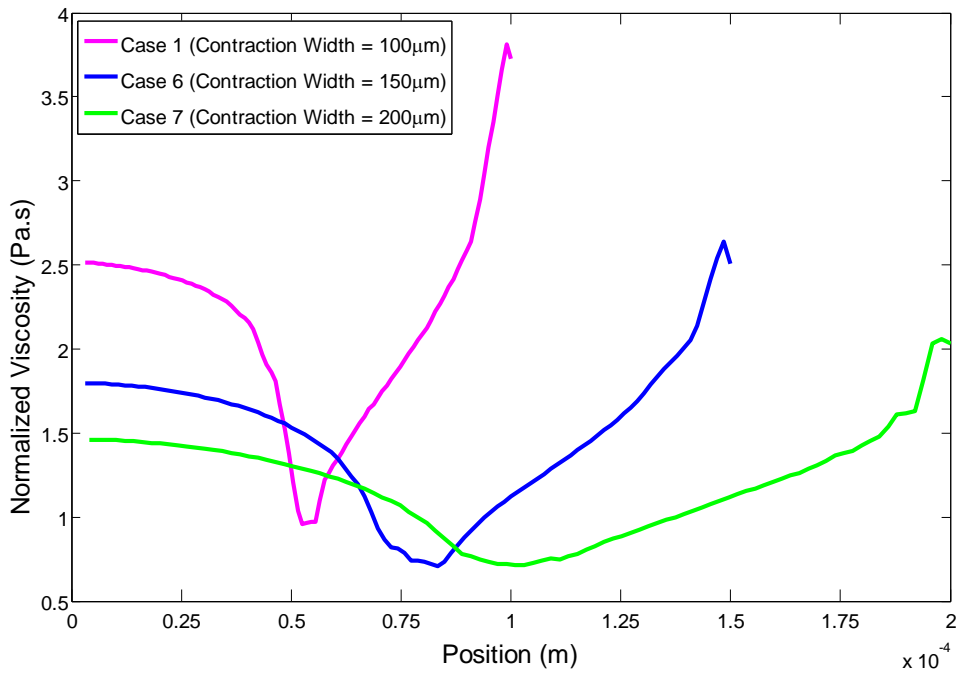
Figure 14. Effect of the contraction width on the viscosity profile across the contraction

28
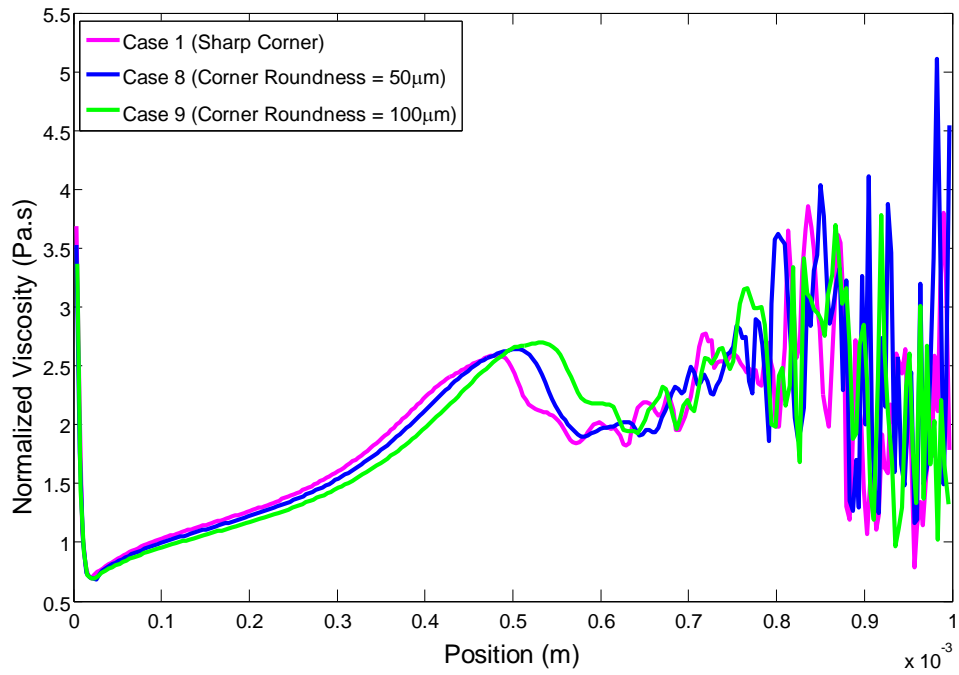
Figure 15. Effect of the corner roundness on the viscosity profile along the Line-1
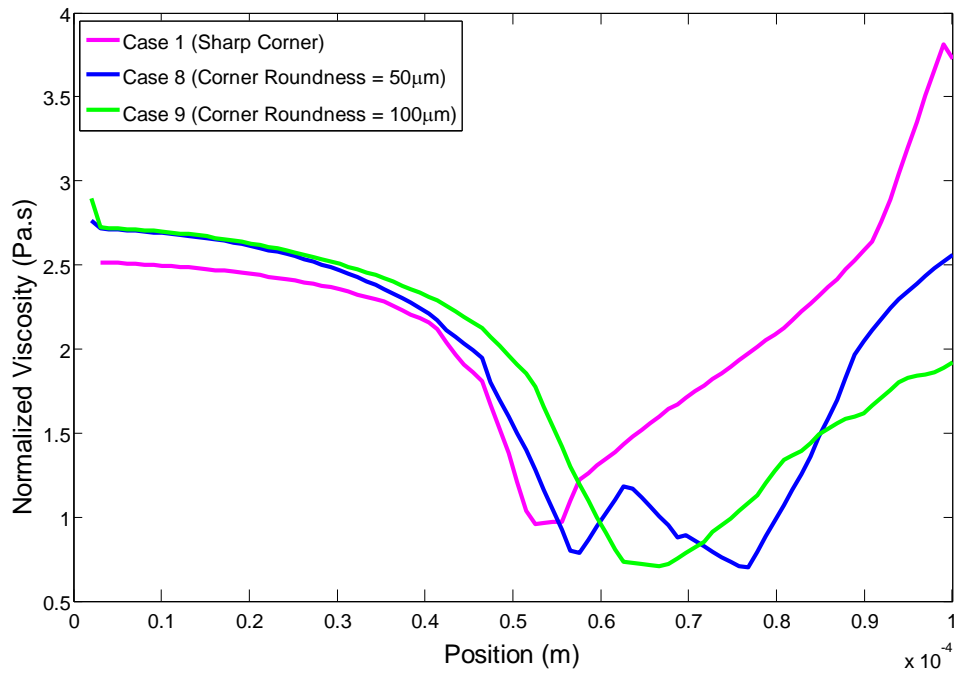
Figure 16. Effect of the corner roundness on the viscosity profile across the contraction

Figure 17 and Figure 18 show the velocity and dynamic pressure contours of the fluid, respectively for case 1. Dynamic pressure increases inside the channel reaching at its maximum close to the exit and at the center, due to the area contraction. Expectedly, velocity also increases inside the channel reaching at its maximum close to the exit due to the dynamic pressure build up, which drives the fluid flow.
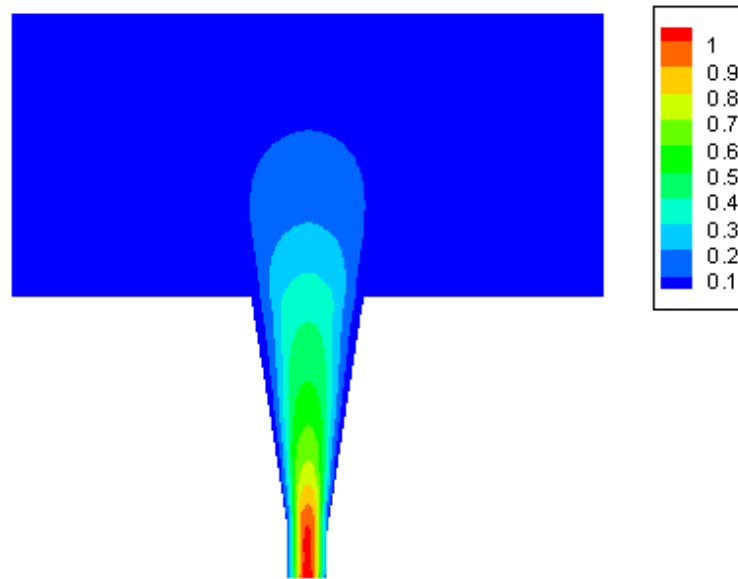
Figure 17. Velocity contours of the mixture
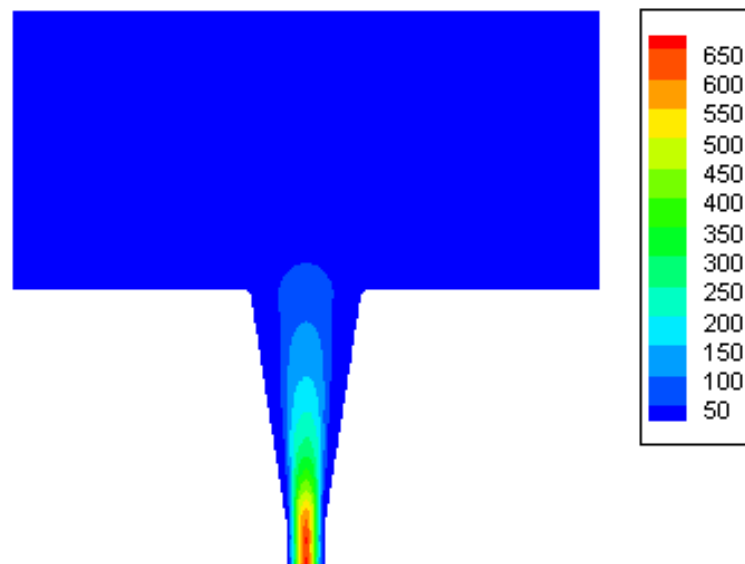
Figure 18. Dynamic pressure contours of the mixture

Viscosity contours of the mixture are given in Figure 19. It can be seen that viscosity is higher at the corners of contraction, inside the channel near the walls. It reaches to the maximum value near to second contraction where the shear rate on the wall is quite high.

The maximum value of viscosity reached to 1.9 Pa.s which is almost 5.4 fold of the zero shear viscosity. This increased viscosity near to the channel exit along brings about the possibility of clogging of the exit over the time. Even if clogging does not occur, fiber diameter may be reduced due to the sticking of the fluid and particles to the walls.
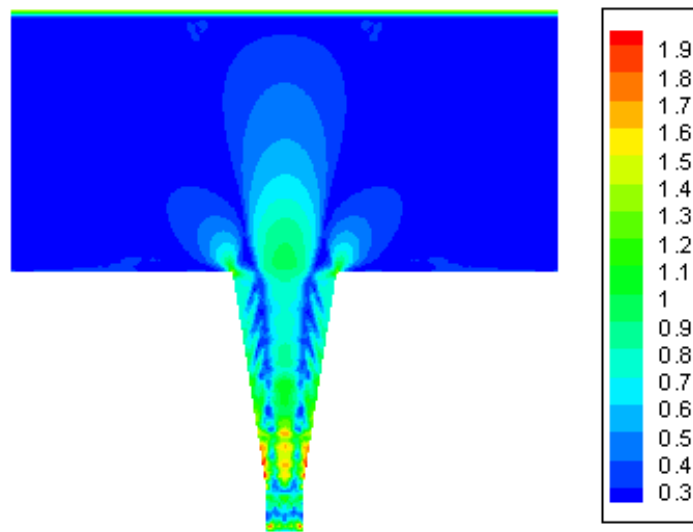
Figure 19. Viscosity contours of the mixture

5.2.2.2. Fluid Velocity

There is a direct relationship between velocity and viscosity of a fluid. Depending on the fluid being Newtonian or non-Newtonian, viscosity profiles change with changing velocity. In order to see the changes in viscosity, we increased velocity gradually and kept all other flow parameters constantly.

Table 3. Different velocities used and their correspondence to mass flow rates

Case Number	Velocity (m/s)	Mass flow rate (kg/s)
1	0.03	0.0185
10	0.06	0.0371
11	0.12	0.0742

It is already known that shear rate is directly proportional to velocity, thus with increasing velocity, shear rate also increases. Recalling once again the Hagen-Poiseuille equation, one should expect higher viscosities, with increased velocity gradients. Considering this, it was expected to see higher viscosities at higher velocities. Figure 20 and Figure 21 show the viscosity profiles varying with velocity, along the Line-1 and Line-2, respectively. Figure 20 shows severe increase in viscosity with increasing velocity, expectedly. Figure 21 also shows a significant increase across the contraction, especially at the edge. For case 11, where velocity was 0.12 m/s, viscosity at the edge was as high as 9 times according to its zero shear viscosity.

Simulations were also done with respectively lower velocities. Figure 22 shows the viscosity contour plot of the case where inlet velocity was 0.0019 m/s. It can be seen from the Figure 22 that very low velocities cause the settlement of particles and fluid as well, on to the walls, so it prevents the flow and fails the production.

From these simulations, varying inlet velocities, it was understood that the velocity is a very critical design parameter for both channel flow and wet spinning process. For the sake of keeping the viscosity low, and prevent severe shear thickening, velocity should be kept low. But at the same time, lower velocities mean lower production rates, thus for big scales of mass production of fibers, velocity is even more significant design parameter.
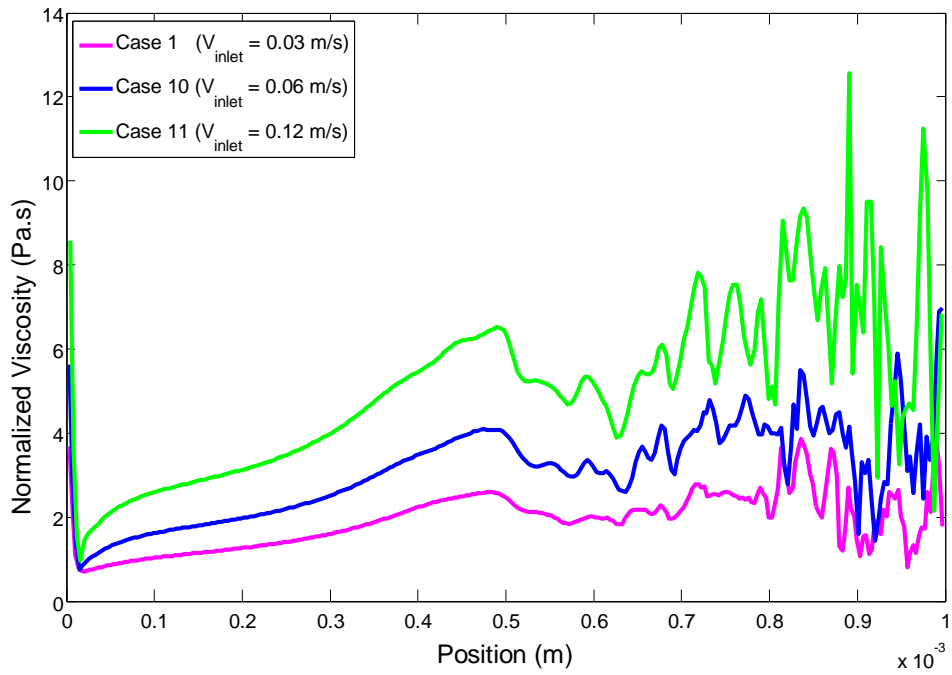
Figure 20. Effect of the velocity on the viscosity profile along the Line-1
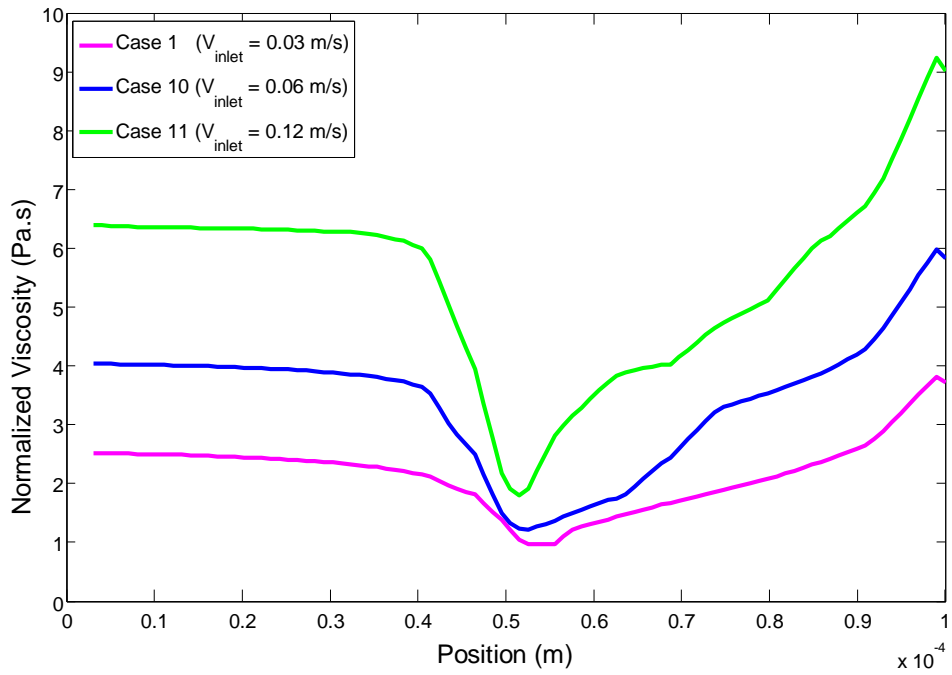
Figure 21. Effect of the velocity on the viscosity profile across the contraction

33

The color scale alongside the figure, from top to bottom:

3.46e-01
3.36e-01
3.27e-01
3.18e-01
3.08e-01
2.99e-01
2.89e-01
2.80e-01
2.71e-01
2.61e-01
2.52e-01
2.42e-01
2.33e-01
2.24e-01
2.14e-01
2.05e-01
1.95e-01
1.86e-01
1.76e-01
1.67e-01
1.58e-01

Figure 22. Viscosity contours of the mixture where inlet velocity boundary condition is used as 0.0019 m/s

CHAPTER 6

CONCLUDING REMARKS

This work has investigated several important parameters that affect the flow behavior of non-Newtonian shear thickening multiphase fluids. Those parameters were geometry of the spinneret and the flow rate. Within the scope of geometry study, reservoir depth, channel length, contraction width and corner roundness were varied. The results showed that depth of the reservoir does not affect the viscosity profile of the fluid whereas the length of the channel has a small influence; nevertheless, none of these two parameters can be considered to possess significant importance. Further results showed that sudden contractions give rise to higher viscosities inside the spinneret due to higher shear rates, and widening the contraction area reduces the increase in the viscosity. It was also found that corners inside the geometry are shear rate concentrating areas, and by rounding the corners, the effect of corner roundness on the viscosit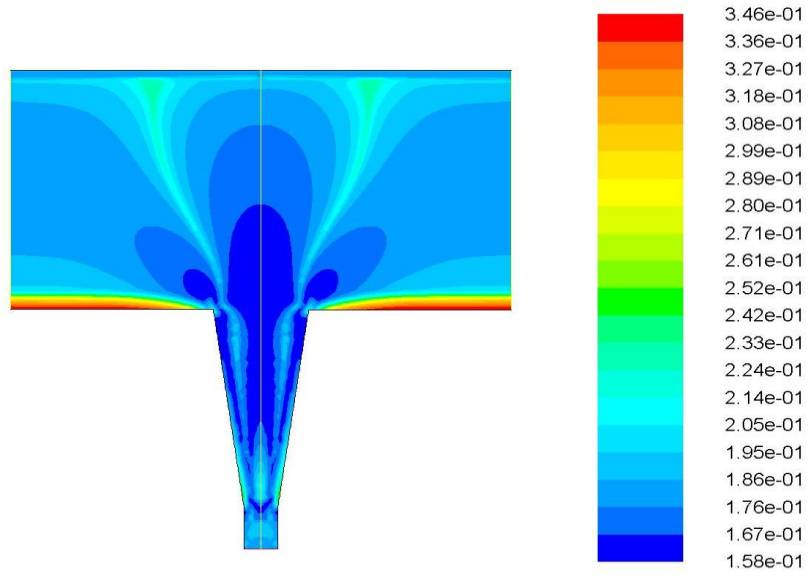y can be alleviated. Another significant outcome of this study is that the higher the flow rate, the viscosity increases more dramatically due to the increasing shear rate while at the lower flow rates, the decrease in viscosity is observed. However, at fairly lower flow rates, very high viscosities were also observed due to the settling.

6.1. Future Work

To further improve the context of this study, the investigation of the particle size and particle loading on the flow behavior inside the spinneret should be investigated. Eulerian-Lagrangian Model and Dense Discrete Phase Model should also be used to be able to test if they can provide additional physics for the problem considered in this study. The geometry without symmetric boundaries should be used in simulations in order to check if buoyancy arising from nanoparticles affects the viscosity and the overall solution since there are some studies in the literature that showed the importance of buoyancy in particulate non-Newtonian flows.

APPENDIX A

As described in section 4.2.3, the fluid used in the simulations was a so-called complex fluid which showed shear thinning below a certain shear rate, and above that shear rate it showed shear thickening. This complex viscosity behavior was fitted to the Carreau fluid model by splitting the data into two parts as shear thinning and shear thickening, and identified to the FLUENT by using a UDF, which was coded in-house by using C programming language. There is the UDF code given below.

```c
# include <udf.h>
# include <math.h>
# include <mem.h>
# include <sg_mphase.h>
# include <cmath.h>
# include <stdio.h>

DEFINE_PROPERTY(D11_PEG200_carreau_visc, c, t)
{
        real strain;
        real visc;
        real eta01, eta0r;
        real eta_inf1, eta_infr;
        real lambda1, lambdar;
        real n1, nr;
        real threshold;
        real cntrl;
        threshold=95.78;
        eta01=0.35517;
        eta0r=0.23937;
```

```
eta_inf1=0;

eta_infr=0;

lambda1=10.4741;

lambdar=0.00562;

n1=0.94445;

nr=1.67844;

strain=C_U_G(c,t)[0];

strain=sqrt(strain*strain);

if (strain<=threshold)

{
        visc=eta_inf1+(eta01-eta_inf1)*pow((1+pow(lambda1*strain,2)),(n1-
1)/2);
}

else

{
        visc=eta_infr+(eta0r-eta_infr)*pow((1+pow(lambdar*strain,2)),(nr-1)/2);
}

return visc;

}
```

REFERENCES

1. Nakamura, A. and N. Akira, *Fiber science and technology*. 2000, Enfield, N.H.: Enfield, N.H. : Science Publishers.
2. Hongū, T. and H. Tatsuya, *New millennium fibers*, ed. G.O. Phillips and M. Takigami. 2005, Cambridge: Cambridge : Woodhead.
3. Elgafy, A. and K. Lafdi, *Carbon nanoparticle-filled polymer flow in the fabrication of novel fiber composites*. Carbon, 2006. **44**(9): p. 1682-1689.
4. Fourné, F. and F. Franz, *Synthetic fibers : machines and equipment, manufacture, properties : handbook for plant engineering, machine design, and operation*. 1999.
5. Masson, J.C., *Acrylic fiber technology and applications*, ed. J.C. Masson. 1995, New York: New York : M. Dekker.
6. Catherall, A.A., J.R. Melrose, and R.C. Ball, *Shear thickening and order–disorder effects in concentrated colloids at high shear rates*. Journal of Rheology (1978-present), 2000. **44**(1): p. 1-25.
7. Marinack, M.C., J.N. Mpagazehe, and C.F. Higgs, *An Eulerian, lattice-based cellular automata approach for modeling multiphase flows*. Powder Technology, 2012. **221**: p. 47-56.
8. Deshpande, A.Y., et al., *Rheology of complex fluids*. 2010, Springer,: New York ; London. p. p.
9. Sochi, T., *Flow of non-newtonian fluids in porous media*. Journal of Polymer Science Part B: Polymer Physics, 2010. **48**(23): p. 2437-2767.
10. Chen, D.T.N., et al., *Rheology of Soft Materials*. Annual Review of Condensed Matter Physics, 2010. **1**(1): p. 301-322.
11. Bender, J. and N.J. Wagner, *Reversible shear thickening in monodisperse and bidisperse colloidal dispersions*. Journal of Rheology (1978-present), 1996. **40**(5): p. 899-916.
12. Wagner, N.J. and J.F. Brady, *Shear thickening in colloidal dispersions*. Physics Today, 2009. **62**(10): p. 27-32.
13. Hoffman, R.L., *Discontinuous and dilatant viscosity behavior in concentrated suspensions. II. Theory and experimental tests*. Journal of Colloid and Interface Science, 1974. **46**(3): p. 491-506.
14. Barnes, H.A., *Shear-Thickening (Dilatancy) in Suspensions of Nonaggregating Solid Particles Dispersed in Newtonian Liquids*. Journal of Rheology, 1989. **33**(2): p. 329-366.
15. Boersma, W.H., J. Laven, and H.N. Stein, *Shear thickening (dilatancy) in concentrated dispersions*. AIChE Journal, 1990. **36**(3): p. 321-332.
16. Xu, D., C.-Y. Liu, and S.L. Craig, *Divergent Shear Thinning and Shear Thickening Behavior of Supramolecular Polymer Networks in Semidilute Entangled Polymer Solutions*. Macromolecules, 2011. **44**(7): p. 2343-2353.
17. Barnes, H.A., *A Handbook of Elementary Rheology*. 2000: University of Wales, Institute of Non-Newtonian Fluid Mechanics.
18. Kroger, M., R. Editor Applied, and editors@appliedrheology.org, *Rheology for Polymer Melt Processing (J. M.-Piau and J.-F. Agassant, Eds.)*. 2000, ETH Zurich; Applied Rheology.
19. Shaw, C.T., *Using computational fluid dynamics*. 1992, New York: Prentice Hall. xviii, 251 p.

20.   Kozic, M., et al., *Numerical simulation of multiphase flow in ventilation mill and channel with louvers and centrifugal separator.* Thermal Science, 2011. **15**(3): p. 677-689.

21.   Pirker, S., et al., *Simulating coarse particle conveying by a set of Eulerian, Lagrangian and hybrid particle models.* Powder Technology, 2010. **204**(2-3): p. 203-213.

22.   Kaushal, D.R., et al., *Flow of mono-dispersed particles through horizontal bend.* International Journal of Multiphase Flow, 2013. **52**: p. 71-91.

23.   Kalteh, M., et al., *Eulerian–Eulerian two-phase numerical simulation of nanofluid laminar forced convection in a microchannel.* International Journal of Heat and Fluid Flow, 2011. **32**(1): p. 107-116.

24.   Kamali, R. and A.R. Binesh, *Numerical investigation of heat transfer enhancement using carbon nanotube-based non-Newtonian nanofluids.* International Communications in Heat and Mass Transfer, 2010. **37**(8): p. 1153-1157.

25.   Ding, Y., et al., *Heat transfer of aqueous suspensions of carbon nanotubes (CNT nanofluids).* International Journal of Heat and Mass Transfer, 2006. **49**(1–2): p. 240-250.

26.   Yajie, R., X. Huaqing, and C. An, *Effective thermal conductivity of nanofluids containing spherical nanoparticles.* Journal of Physics D: Applied Physics, 2005. **38**(21): p. 3958.

27.   Heris, S.Z., M.N. Esfahany, and G. Etemad, *Numerical Investigation of Nanofluid Laminar Convective Heat Transfer through a Circular Tube.* Numerical Heat Transfer, Part A: Applications, 2007. **52**(11): p. 1043-1058.

28.   Eesa, M. and M. Barigou, *CFD analysis of viscous non-Newtonian flow under the influence of a superimposed rotational vibration.* Computers & Fluids, 2008. **37**(1): p. 24-34.

29.   Sahu, A.K., R.P. Chhabra, and V. Eswaran, *Two-dimensional laminar flow of a power-law fluid across a confined square cylinder.* Journal of Non-Newtonian Fluid Mechanics, 2010. **165**(13-14): p. 752-763.

30.   Manzar, M.A. and S.N. Shah, *Particle distribution and erosion during the flow of newtonian and non-newtonian slurries in straight and coiled pipes.* Engineering Applicationd of Computational Fluid Mechanics, 2009. **3**(3): p. 25.

31.   Hicks, C.I., et al., *The shear rheology of bread dough: Analysis of local flow behaviour using CFD.* Food and Bioproducts Processing, 2012. **90**(3): p. 361-369.

32.   Norton, T. and D.-W. Sun, *Computational fluid dynamics (CFD) – an effective and efficient design and analysis tool for the food industry: A review.* Trends in Food Science & Technology, 2006. **17**(11): p. 600-620.

33.   *Fluent User's Guide 14.0*, I. ANSYS, Editor. 2011.

34.   Gidaspow, D., R. Bezburuah, and J. Ding, *Hydrodynamics of circulating fluidized beds: Kinetic theory approach.* 1991. Medium: ED; Size: Pages: (8 p).

35.   Syamlal, M., W. Rogers, and T.J. O`Brien, *MFIX documentation theory guide*, in *Other Information: PBD: Dec 1993*. 1993. p. Medium: ED; Size: 49 p.

36.   Huilin, L., et al., *Hydrodynamic simulation of gas–solid flow in a riser using kinetic theory of granular flow.* Chemical Engineering Journal, 2003. **95**(1–3): p. 1-13.

37.   Gibilaro, L.G., et al., *Generalized friction factor and drag coefficient correlations for fluid-particle interactions.* Chemical Engineering Science, 1985. **40**(10): p. 1817-1823.

38.   Lun, C.K.K., et al., *Kinetic theories for granular flow: inelastic particles in Couette flow and slightly inelastic particles in a general flowfield.* Journal of Fluid Mechanics, 1984. **140**: p. 223-256.

39.   Ozel, B.G., et al., *Experimental study on the rheology of anisotropic, flocculated and low volume fraction colloids.* Korea-Australia Rheology Journal, 2014. **26**(1): p. 105-116.

40.   Eesa, M. and M. Barigou, *CFD investigation of the pipe transport of coarse solids in laminar power law fluids.* Chemical Engineering Science, 2009. **64**(2): p. 322-333.

41.   Bird, R.B., W.E. Stewart, and E.N. Lightfoot, *Transport Phenomena.* 2001: Wiley.